Corrosion Science 77 (2013) 151–163

Contents lists available at ScienceDirect

Corrosion Science

journal homepage: www.elsevier.com/locate/corsci

The role of aluminum distribution on the local corrosion resistance of the microstructure in a sand-cast AM50 alloy

Mohsen Danaie [a,*], Robert Matthew Asmussen [b], Pellumb Jakupi [b], David W. Shoesmith [b], Gianluigi A. Botton [a]

[a] Department of Materials Science and Engineering, Brockhouse Institute for Materials Research and Canadian Centre for Electron Microscopy, McMaster University, Hamilton, Ontario, Canada
[b] Department of Chemistry and Surface Science Western, Western University, London, Ontario, Canada

ARTICLE INFO

Article history:
Received 19 April 2013
Accepted 25 July 2013
Available online 2 August 2013

Keywords:
A. Magnesium
A. Alloy
B. TEM
B. STEM

ABSTRACT

Site-specific analytical electron microscopy was performed on a corroded sand-cast AM50 alloy. Areas close to partially divorced eutectic were the regions with less corrosion damage. The corrosion product layer in these areas consisted of a columnar section of predominantly amorphous MgO. At the alloy interface, an aluminum-rich layer was identified. Electron energy-loss spectroscopy suggests this layer is metallic in character. The corrosion product film on the primary α-Mg grains possessed a bi-layer morphology: a thin columnar film and a thicker, porous sub-layer. The formation of the Al-rich layer depends on the Al content in solid solution at a specific location.

1. Introduction

Magnesium alloys with low density, high stiffness, and good machinability and castability are generating attention in the automotive and aerospace industries, although their share of the market is still dwarfed by various aluminum alloys [1]. Two main drawbacks have hindered the more widespread application of Mg alloys: poor corrosion properties and poor creep behavior. The latter issue, mostly linked to the presence of low melting point intermetallic phases on grain boundaries, has been successfully addressed by modifying the alloy composition [2]. Poor corrosion resistance remains the major impediment to Mg alloy development.

Early improvements in corrosion properties were achieved by producing alloys with reduced impurity levels [1]. Lowering the concentrations of iron, nickel, and copper, which all act as cathodes within the alloy, was crucial in this context [3–5]. Among the alloying elements, there is a strong consensus that Al has a beneficial effect on overall corrosion resistance. Lindström et al. [6] reported that in high humidity environments, in the absence of CO_2, the general corrosion rate is reduced with increasing Al content (in the order; AZ91 < AM60 < AM20), and Mathieu et al. [7] demonstrated this electrochemically on single-phase α-Mg (solid solution of Al in Mg) electrodes containing various Al concentrations. They reported a linear increase in corrosion potential with increasing Al content in solid solution. Higher concentrations of Al in solid solution, as compared in the alloys AZ31, AZ80, and AZ91D, is demonstrated to result in enhanced corrosion resistance in a humid hot air environment [8]. A higher Al content has also been shown to be beneficial in reducing the corrosion rate of rapidly solidified Mg binary alloys [9], and the α-Mg grains in the die-cast AZ91D alloy [10].

Another important feature in the corrosion behavior of the Mg–Al alloys is the microstructure and the distribution of the intermetallic phase, β-$Mg_{17}Al_{12}$. When the number of β-$Mg_{17}Al_{12}$ regions is lower in population, compared to the α-Mg grains, these areas may act as microgalvanic cathodes and accelerate the local corrosion rate [11–13]. A more uniform and dense distribution of the β-$Mg_{17}Al_{12}$ phase, on the other hand, could yield an improved corrosion resistance. Pardo et al. [14] reported a reduced rate of corrosion of AZ80 and AZ91D, in 3.5 wt.% NaCl solution, compared to commercially pure Mg and AZ31. This improvement was attributed to the development of an Al-rich layer at the interface between metal and corrosion products, whereas in the case of AZ91D, this was correlated with the presence of a continuous network of eutectic β-$Mg_{17}Al_{12}$ phase along the grain boundaries. Similar trends were observed for the corrosion of the same series of alloys, i.e. commercial Mg, AZ31, AZ80, and AZ91D, in salt fog environment [15].

Microscopic characterization of the corrosion film on Mg alloys can lead to identification of the weakest microstructural links and information on the active corrosion mechanisms. In pioneering studies by Nordlien et al. [16–18], transmission electron micros-

* Corresponding author. Tel.: +1 905 525 9140x24862; fax: +1 905 521 2773.
E-mail addresses: danaiem@mcmaster.ca (M. Danaie), gbotton@mcmaster.ca (G.A. Botton).

0010-938X/$ - see front matter © 2013 Elsevier Ltd. All rights reserved.
http://dx.doi.org/10.1016/j.corsci.2013.07.038

copy (TEM) was used to examine the morphology of the oxide/hydroxide layer on both pure and alloyed Mg. The corrosion product on Mg–Al alloys exhibited a three-layer structure [18], with the layer closest to the alloy having a higher Al content, with respect to the bulk metal. X-ray photoelectron spectroscopy (XPS) demonstrated the accumulation of Al^{3+} species on the corroded surface of Mg–Al alloys [19–21]. This is interpreted as percolation of amorphous Al_2O_3 within the $MgO/Mg(OH)_2$ corrosion layer [18], resulting in the observed enhanced corrosion resistance. It has also been claimed that Al-enrichment can be an artifact caused by sputter cleaning of the initial alloy surface, due to the higher sputtering rate of Mg [22].

In this study, our objective is to characterize the corrosion film formed on the Mg–Al alloy (AM50) at locations adjacent to the primary α-Mg grains and close to the eutectic microstructure in the alloy. It has been shown that the casting technique has a significant impact on the corrosion mechanism of this alloy, with high-pressure die-casting yielding better corrosion properties [23]. Our focus in the present study is on the sand-cast version of this alloy. Previous studies on the corrosion layer on Mg alloys have mainly focused on broad-beam techniques, like XPS, that yield an averaged signal with low spatial resolution. Other studies employing electron microscopy and X-ray energy dispersive spectroscopy (XEDS) were performed predominantly on ultra-microtomed specimens, which do not allow selection of specific areas present in the alloy [16–18]. Using a focused ion beam for TEM sample preparation, our goal is to characterize the corrosion product layer in the vicinity of the main microstructural features in the alloy AM50. This allows us to examine the potentially corrosion resistant properties of the various constituents within the microstructure.

2. Experimental procedure

Sand-cast AM50 alloy samples were provided by General Motors staff at the India Science Lab in the form of a cylindrical ingot. The chemical composition is presented in Table 1, and complies with the ASTM B275 standard for this alloy [24]. The ingot was cut into cubic pieces with dimensions of 1.5 cm × 1.5 cm × 1 cm. The samples were directly polished, without embedding or mounting. The initial mechanical grinding was performed on SiC abrasive paper (up to 800 grit), using water as coolant. The grinding surface was covered with metallography wax in order to minimize embedding of the SiC particles within the soft magnesium alloy. Subsequently, polishing was performed using an oil-based diamond paste (3 μm) on a Struers MD-Dur polishing surface. A mixture of propylene glycol (25 vol.%) and ethanol was used as a lubricant during polishing, in order to avoid any water exposure of the polishing surface from this stage onwards. We only used anhydrous ethanol for rinsing and cleaning after this step. Final polishing on the sample was carried out with colloidal silica. Bulk colloidal silica (SYTON-HT50) was mixed with propylene glycol (1:2 ratio) and used fresh on Struers MD-Chem surface. Polishing was continued until the 3 μm scratches were all removed from the surface. The sample was subsequently sonicated in anhydrous ethanol for cleaning and then dried in air.

The microstructure of the as-cast alloy was studied at low magnification using a light microscope (Zeiss Axioplan 2 Imaging microscope, with a Hal 100 halogen lamp) and at higher magnification with a dual-beam scanning electron microscope/focused ion beam (SEM/FIB) (Zeiss NVision 40) equipped with an X-ray energy-dispersive spectrometer (XEDS – Oxford Inca, Silicon drift detector). The as-cast microstructure was characterized by transmission electron microscopy (TEM) on electropolished thin foils. After mechanical thinning to ~80 μm thickness, disks (3 mm in diameter) were punched. A Struers Tenupol-5 twin jet electropolishing unit was then used to thin and perforate the samples. A slightly modified electropolishing recipe [25], comprising 5% $HClO_4$, 15% ethylene glycol and 80% methanol electropolishing solution was used at 20 V and −40 °C. The TEM foils were then further thinned by ion milling. A Gatan precision ion polishing system (PIPS) was used at 3 keV beam energy, with an incidence angle of 4°.

Corrosion studies were performed on polished specimens immersed in an aerated 1.6 wt.% NaCl (reagent grade, 99% assay) solution at room temperature. This concentration of solution was used, in accordance with General Motors procedures, in order to simulate corrosion under road conditions [23,26]. The sample was periodically removed from the solution, rinsed and sonicated in anhydrous ethanol and dried. Surface topography was analyzed using confocal laser scanning microscopy (CLSM) and XEDS. The CLSM results have been published elsewhere [27].

After 96 h of total immersion, the alloy was analyzed in more detail. Two locations representative of the general microstructure were chosen for TEM analyses. Caution was taken not to alter the surface film structure during FIB preparation. At each region, an ~1 μm-thick tungsten protective film was deposited, initially through electron-beam assisted deposition (known not to damage the surface) and subsequently through ion-beam assisted deposition. Thinning of the FIB lamella was performed in steps with an ion beam reduced in energy from 30 kV to 5 kV. Final polishing was performed at 1 kV accelerating voltage. The FIB samples were stored in a vacuum desiccator immediately after preparation until TEM analyses were performed. Microscopic characterization was performed on an FEI Titan 80-300 (scanning) transmission electron microscope, (S) TEM, equipped with an X-ray energy-dispersive spectrometer (XEDS – Oxford Inca, Si(Li) detector) and a Gatan Image Filter (GIF) electron energy-loss spectrometer (EELS). The TEM accelerating voltage was set at 300 kV. The energy spread of the primary electron beam, measured at the full width at half maximum of the zero-loss peak in vacuum was 0.7 eV or better. Electron beam damage was minimized by conducting analyses on a cryogenically cooled sample holder (T = 95 K).

Two complementary techniques were applied: (a) selected area diffraction (SAD) in parallel beam TEM mode along with bright-field (BF) imaging, and (b) analytical microscopy with EELS and XEDS using the spectrum imaging technique in STEM mode, i.e. STEM/EELS and STEM/XEDS. The first technique provided the local crystal structure of the phases present, and was performed first to monitor any artifacts caused by electron beam irradiation. Subsequently, in stage (b), STEM/XEDS maps were used to confirm the existence of various atomic species. STEM/EELS spectrum images, both in low-loss and core-loss, were acquired to check the data from XEDS measurements and also to study the chemistry of the coexisting phases. In the low-loss region of the EEL spectra (0–50 eV energy loss) the volume plasmon excitation peaks were used to map and identify the various phases present. Assuming a free-electron model for valence electrons in the solid, the volume plasmon excitation energy (E_p) can be expressed as [28]

$$E_p = (28.82)(z\rho/A)^{0.5}\ \text{eV} \quad (1)$$

where z is the number of valence electrons per molecule, ρ is the density (g/cm^3), and A is the molecular weight. This model only provides a good estimate for E_p of the phases with metallic bonding character.

Table 1
Composition of the AM50 magnesium alloy used for this study.

Major elements (wt.%)				Minor elements (ppm-weight)				
Al	Mn	Zn	Si	P	Cu	Fe	Ni	Cr
4.42	0.29	0.09	0.02	56	23	8	4	3

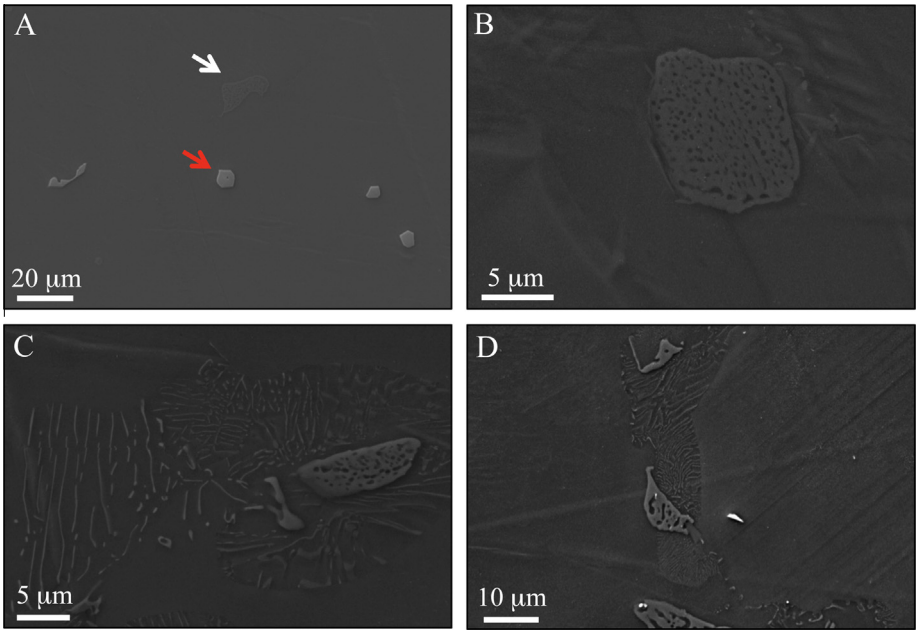

Fig. 1. Morphology of various phases present in sand-cast AM50 alloy: (A) large precipitates of Al–Mn (red arrow) and a partially divorced eutectic (white arrow), (B) a partially divorced eutectic, (C) lamellar microstructure corresponding to a discontinuous precipitation reaction surrounding a partially divorced eutectic, and (D) primary α-Mg grains, eutectic microstructure, and a region with lamellar precipitates of β-$Mg_{17}Al_{12}$ between them. (For interpretation of the references to color in this figure legend, the reader is referred to the web version of this article.)

A high-angle annular dark field (HAADF) detector was used in the STEM mode to form images from electrons scattered at high angles. The contrast observed in the HAADF images is mainly due to variation in the atomic number (Z), elements with a higher Z yielding a higher intensity. The commercial software DigitalMicrograph (from Gatan) was used for EELS and spectrum imaging data analysis. JEMS software was used to simulate electron diffraction patterns. For XEDS data analysis, the commercial software INCA (Oxford Instruments) was used.

3. Results

3.1. Microstructure of the as-cast state

The microstructure of the sand-cast AM50 alloy in the as-polished state is shown in Fig. 1. The secondary phases and precipitates are clearly visible, Fig. 1(A). The white arrow in this figure points to a partially divorced eutectic microstructure. This microstructure contains large eutectic β-$Mg_{17}Al_{12}$ phase and islands of

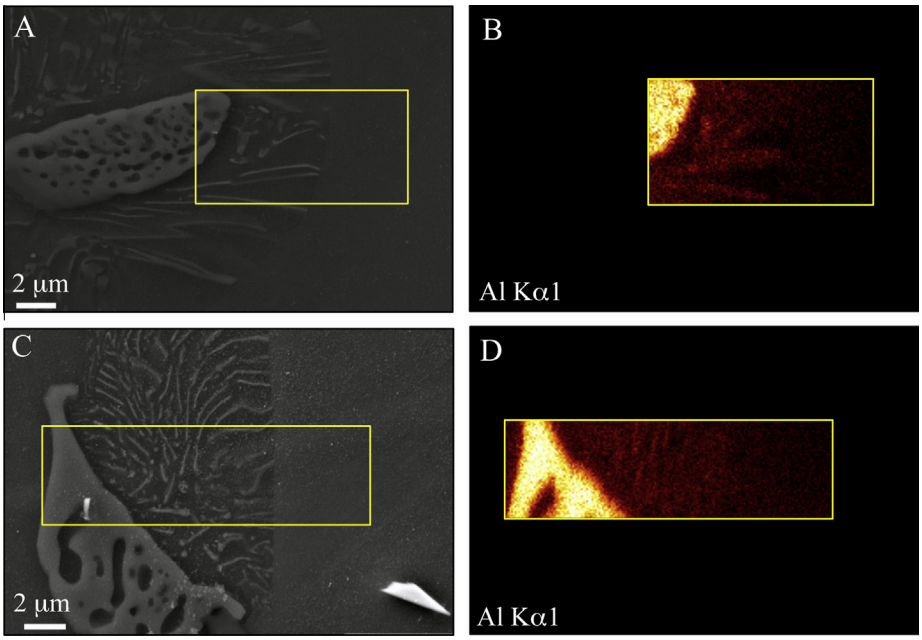

Fig. 2. Two areas (A) and (C) containing primary α-Mg, lamellar precipitates of the β phase, and partially divorced eutectic. XEDS aluminum map of the marked regions are presented in (B) and (D), respectively.

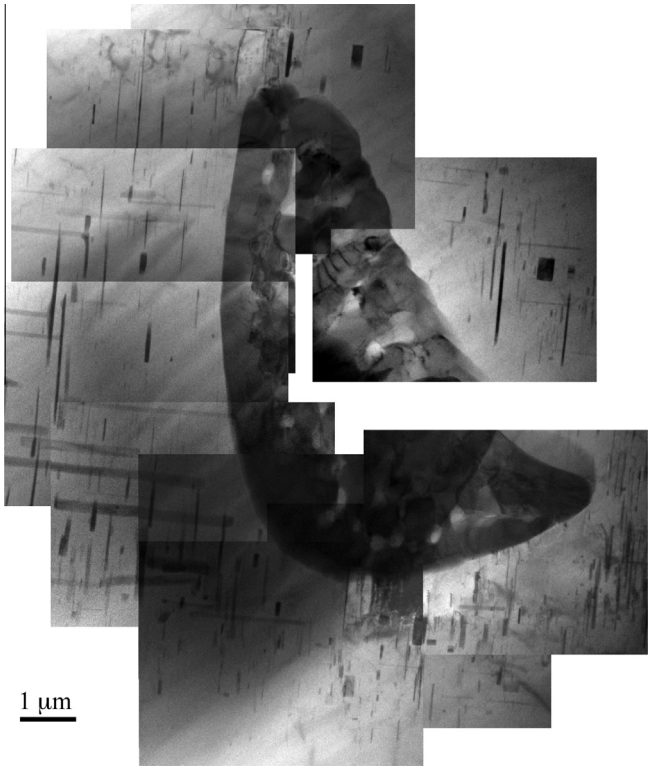

Fig. 3. A collage of bright field TEM micrographs showing the distribution of the β-Mg17Al12 precipitates surrounding a partially divorced eutectic microstructure.

the residue eutectic Mg scattered inside, Fig. 1(B). A lamellar morphology is also occasionally present in the proximity of the partially divorced eutectics, Fig. 1(C) and (D). The lamellar structure, neighboring the partially divorced eutectic, is indicative of a discontinuous precipitation reaction to form Mg and β-$Mg_{17}Al_{12}$ from eutectic Mg grains rich in Al, after completion of solidification [29]. This type of precipitation and morphology are observed at slow cooling rates, as is the case with the sand cast alloy. Beside the β-$Mg_{17}Al_{12}$ structures, there are precipitates with polygonal morphologies. The red arrow in Fig. 1(A) indicates one of these precipitates. The major constituents of these precipitates are Al and Mn, with minor contributions of Si and Fe. Since there is a variety of intermetallic phases in the Al–Mn system [30], we refer to the precipitates with similar morphology as Al–Mn precipitates.

Even though the solubility of Al in Mg at the eutectic temperature (436 °C) is 12 wt.% (11.5 at.%) [31], the eutectic morphology is commonly observed in Mg–Al alloys with Al concentrations as low as 2 wt.% [32]. This can be attributed to the slower diffusion of solute atoms in the solid phase, away from the solidification front, compared to their faster diffusion in the liquid phase [31]. This can also cause significant coring and segregation in the solid phase, with respect to the Al solute atom distribution. At constant solute concentration (Al and Zn), the cooling rate determines the morphology of the eutectic microstructure [28], with faster cooling rates yielding a more divorced eutectic, with fewer Mg islands within the eutectic β-$Mg_{17}Al_{12}$ phase. For instance, in an alloy with a similar composition, a fully divorced eutectic has been shown to form when high-pressure die-casting (HPDC), with a faster cooling rate, is used for solidification [33].

Areas from Fig. 1(C) and (D) are shown at higher magnification in Fig. 2(A) and (C), respectively. Two-dimensional XEDS Al maps of the three microstructural domains, i.e., a primary α-Mg grain, an area with lamellar precipitation of β-$Mg_{17}Al_{12}$, and finally the partially divorced eutectic, are presented in Fig. 2(B) and (D). In both areas the primary α-Mg grain has the lowest Al content, and the areas surrounding the partially divorced eutectic have significantly higher Al content. This gives rise to the discontinuous precipitation of the β phase, with (Mg) solid solution in between. A mosaic view of TEM bright-field micrographs shows the partially divorced

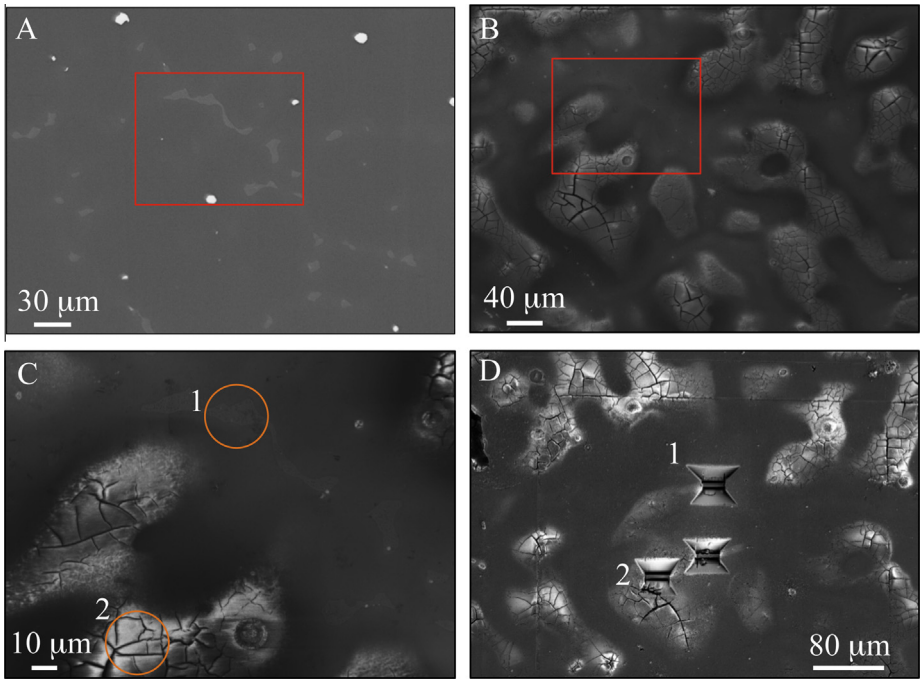

Fig. 4. (A) Area of interest in the as-polished state, prior to immersion. (B) Same area after 96 h of immersion in 1.6 wt.% NaCl solution. The red boxes in (A) and (B) roughly mark the same region in the microstructure. (C) is a higher magnification view of the area of interest with the two locations marked that were chosen for FIB sample preparation. (D) The three representative areas selected in (C), after the FIB samples have been lifted out. (For interpretation of the references to color in this figure legend, the reader is referred to the web version of this article.)

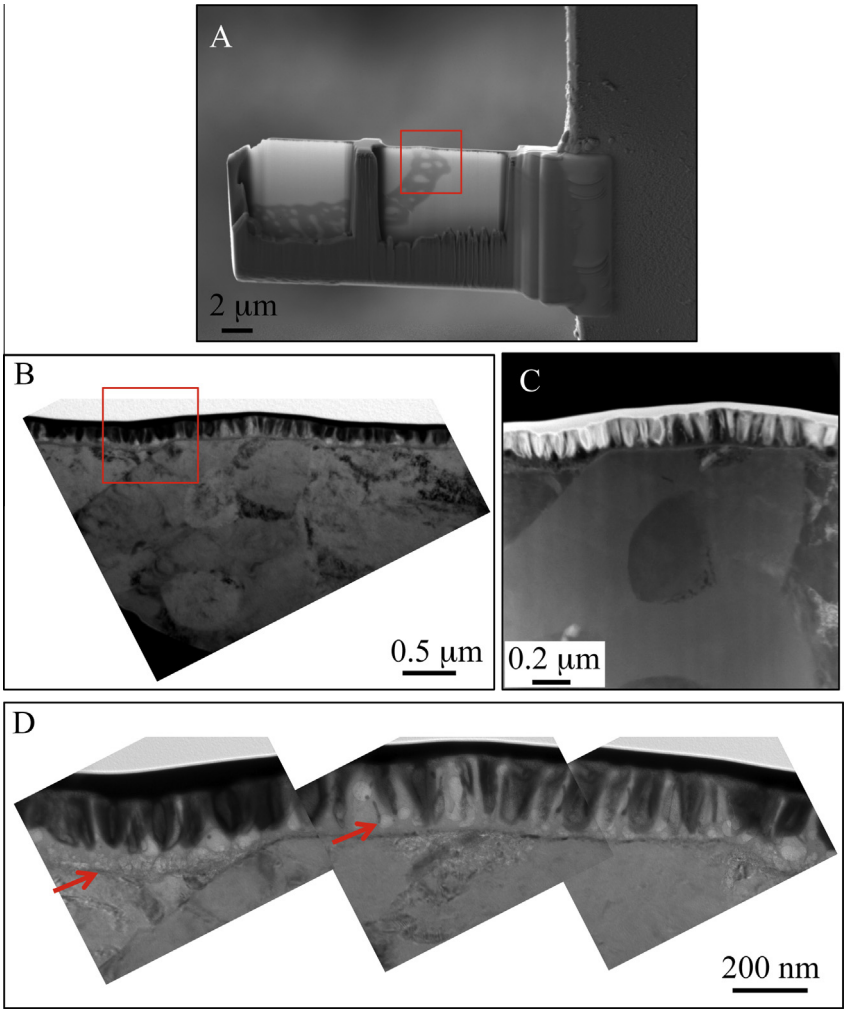

Fig. 5. (A) The FIB sample from area 1, containing the partially divorced eutectic. (B) Bright field TEM micrograph showing an area marked with the box in (A). (C) Same area in STEM HAADF imaging mode. (D) A higher magnification TEM-BF view of the marked area in (B).

eutectic is surrounded by an array of β-$Mg_{17}Al_{12}$precipitates, Fig. 3. These precipitates have grown with two distinct habit planes with respect to the matrix and there is a depleted zone in the proximity of the eutectic structure. Studies on similar systems (Ref. [34] and citations therein) indicate that the precipitation of β-$Mg_{17}Al_{12}$ (BCC) in the Mg matrix (HCP) generally follows the Burgers orientation relationship (OR), i.e. $(0001)_{HCP}||(011)_{BCC}, [2\bar{1}\bar{1}0]_{HCP}||[1\bar{1}1]_{BCC}$, with the basal plane, $(0001)_{HCP}$, as the habit plane.

3.2. Characterization of the corroded state

Fig. 4(A) presents a low magnification SEM micrograph of an area on the as-polished alloy. The main features of the microstructure can be identified based on the results in Section 3.1. Partially divorced eutectic regions and Al–Mn precipitates, appearing with higher intensity can be clearly observed. Al-rich regions, containing lamellar β-$Mg_{17}Al_{12}$ precipitates surrounding the eutectics are not visible at this magnification. Additionally, the primary α-Mg grains are not visible in the absence of etching. The same region after 96 h of immersion in an aqueous solution of 1.6 wt.% NaCl, is shown in Fig. 4(B) and (C). The α-Mg region exhibits significant corrosion damage and is covered with superficially cracked corrosion product. The Al–Mn precipitate, Fig. 4(C), is surrounded by an apparently ruptured spherical section of corrosion products. Two areas, 1 and 2 in Fig. 4(C), each containing a significant microstructural feature were chosen for TEM analyses. Area 1 is in the vicinity of the partially divorced eutectic and area 2 is within a primary α-Mg grain. Fig. 4(D) shows the locations from which FIB sections were extracted. The unnumbered section was cut at the location of an Al–Mn intermetallic but is not discussed here.

3.2.1. Area 1 – Close to a partially divorced eutectic microstructure

Fig. 5(A) shows the FIB sample cut from area 1 and indicates the subsurface extension of the partially divorced eutectic. The area marked with the red box in (A) is presented at higher magnification as a bright field TEM image, Fig. 5(B), and a STEM-HAADF image, Fig. 5(C). The β-$Mg_{17}Al_{12}$ phase appears with higher intensity in the HAADF image due to the higher average atomic number of this phase compared to the Mg matrix. The framed area in Fig. 5(B) is magnified in Fig. 5(D). The columnar morphology of the outer layer of the film is clearly observed and appears as a bright band in the HAADF image due to the deposition of W as a protective layer during sample preparation. The cellular regions, marked in Fig. 5(D) with two arrows in two locations are attributed to electron beam irradiation [18].

Fig. 6(A) highlights an area of the columnar corrosion product layer chosen for SAD, and Fig. 6(B) presents a higher magnification. The diffraction pattern, Fig. 6(C), demonstrates that the only crystalline phase, beside the Mg base metal, is MgO. The dark-field micrograph in Fig. 6(D) shows that the MgO has an extremely fine

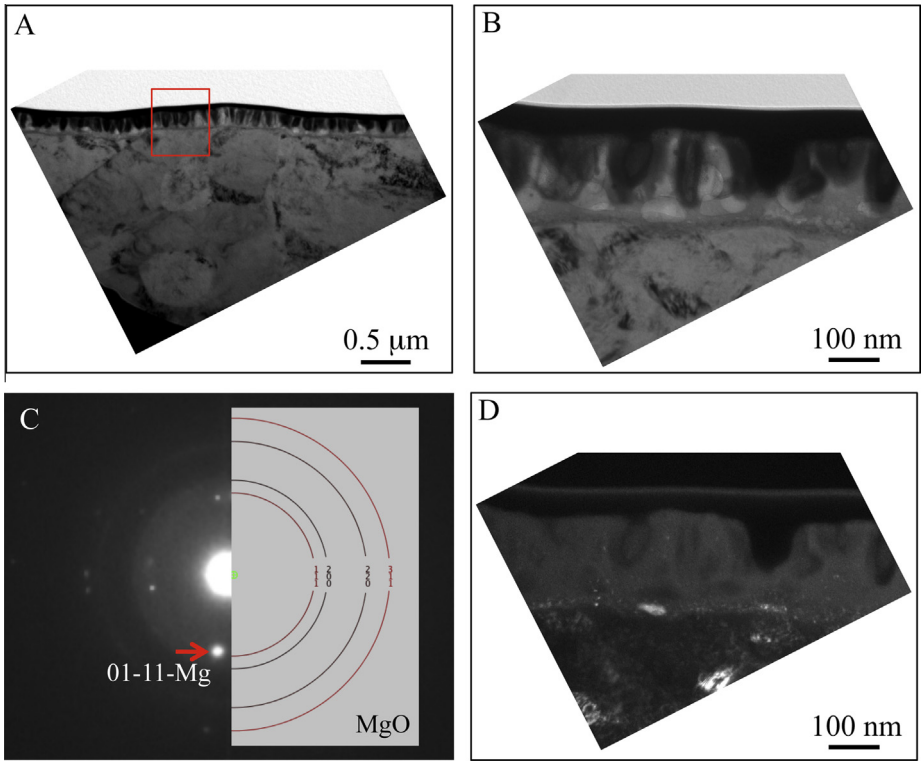

Fig. 6. (A) Low magnification view of the FIB section from area 1. The area of interest is marked by the red box. (B) Bright field TEM image of the marked area in (A). (C) SAD from the same area, along with the ring pattern simulation of MgO. (D) Dark field micrograph from a section of the diffraction rings. (For interpretation of the references to color in this figure legend, the reader is referred to the web version of this article.)

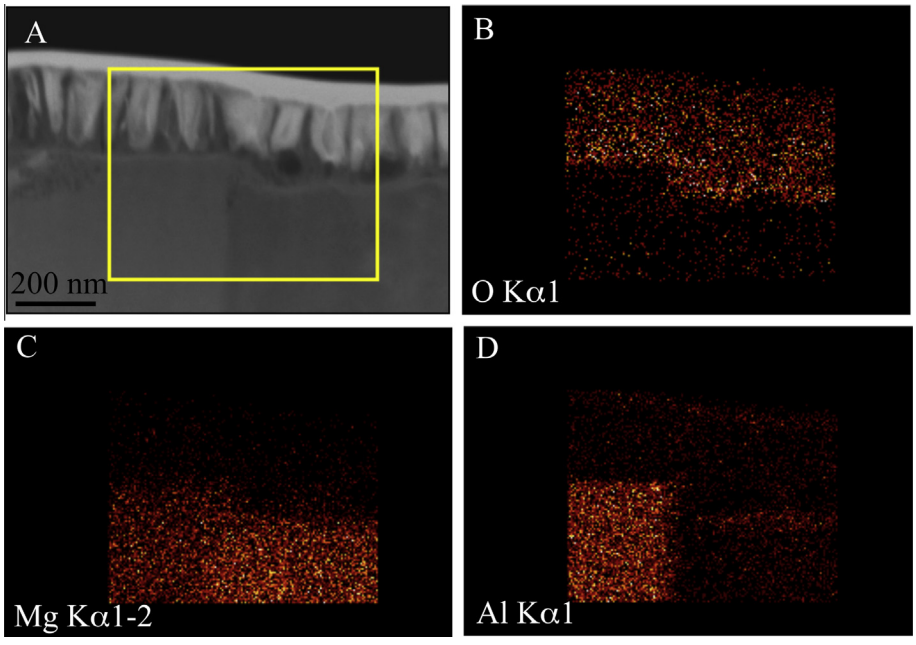

Fig. 7. (A) STEM-HAADF image from the area 1 FIB sample (Fig. 4D). The XEDS elemental maps were acquired from the box in this micrograph. XEDS maps of: (B) O, (C) Mg, and (D) Al.

grain size with the majority of grains located close to the base of the corrosion layer. This is consistent with recently published results on corroded commercially pure Mg [35]. The crystalline MgO coexists with an amorphous phase, as shown from the broad diffuse rings in the diffraction pattern and as reported in the literature [18].

Fig. 7 presents XEDS elemental maps acquired from the region on the right edge of the eutectic β-phase region indicated in Fig. 5(A). The area analyzed is marked in Fig. 7(A). The oxygen map, Fig. 7(B), highlights the location of the surface film with respect to the substrate alloy. As expected, a strong Al signal is obtained for the β-phase, Fig. 7(D). Additionally, an enhanced Al

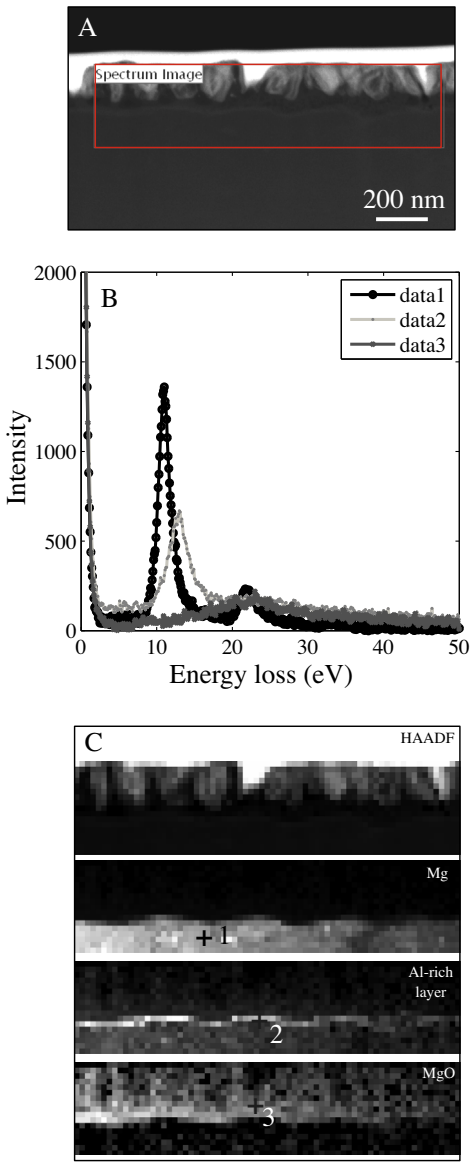

Fig. 8. (A) STEM-HAADF image of the surface layer of area 1. (B) Three cases of the low-loss EEL spectra (corresponding to the locations marked in section C). (C) Top image is the HAADF signal, the image with marker #1 is an intensity map of the energy range of 10.1–12.1 eV (Mg), the image with marker #2 is a map from the range 12.9–13.9 eV (Al-rich layer), and the image with #3 is the map of the range 22.3–33.4 eV (MgO).

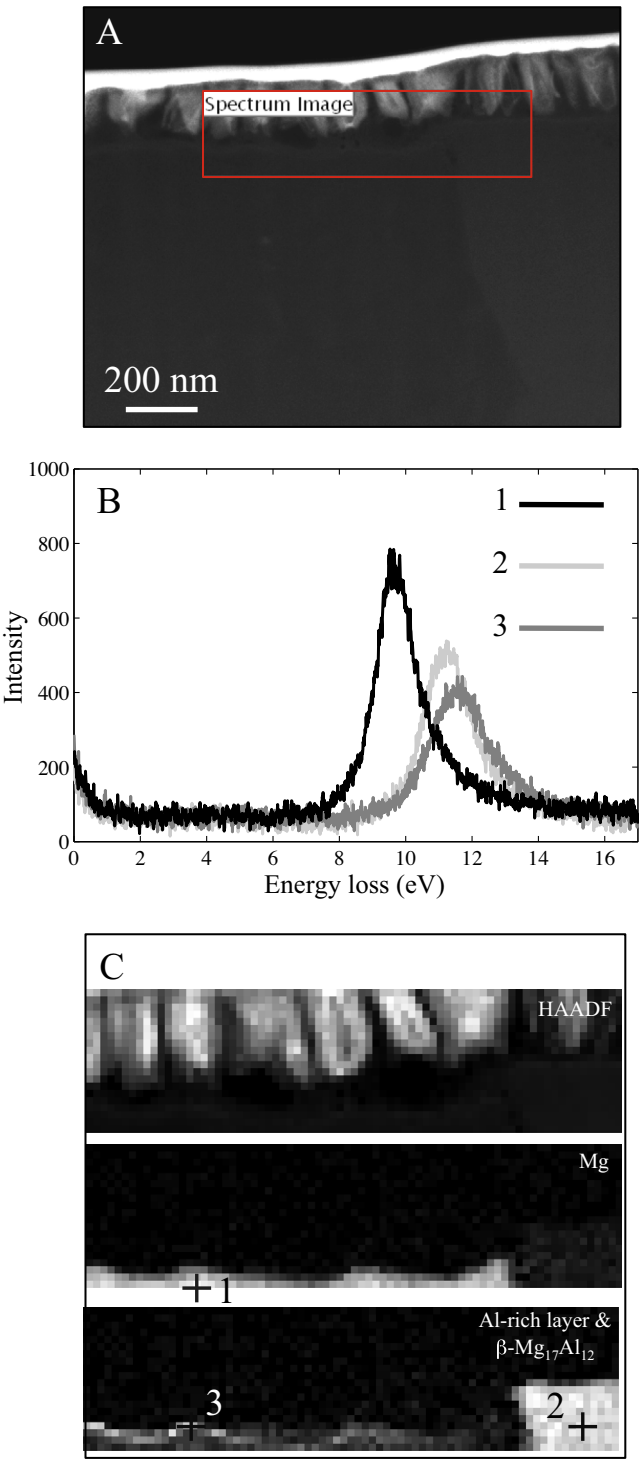

Fig. 9. (A) STEM-HAADF image of the surface layer of area 1. (B) Three cases of the low-loss EEL spectra (corresponding to the locations marked in section C). (C) Top image is the HAADF signal, the image with marker #1 is an intensity map of the energy range of 9.2–10.2 eV (Mg), the bottom image, with markers #2 and #3, is a map from the range 11.1–12.1 eV (Al-rich layer and β-phase).

signal is observed for a thin layer at the surface of the adjacent eutectic Mg grain, Fig. 7(D). The apparent slight enhancement of the Al signal on the outside of the oxide is an artifact arising from the increased background due to the presence of W in the protective layer. The presence of this Al-rich layer was confirmed by a similar analysis on the left edge of the β-phase region (data shown in the supplementary section, Fig. S.1).

To further investigate the nature of this Al-rich layer, we performed low-loss and core-loss EELS measurements. Fig. 8(A) shows a STEM-HAADF image of the surface film, with the analyzed area identified in the frame. Three examples of low-loss EEL spectra, recorded at the locations designated with cross hairs in Fig. 8(C), are shown in Fig. 8(B). The top image in Fig. 8(C) shows the HAADF signal recorded simultaneously with the EELS spectra. The map in Fig. 8(C), labeled 1, shows the intensity map for Mg and spectrum 1 in Fig. 8(B) is the expected volume plasmon peak for metallic Mg (10.7 eV) [36,37]. The image in Fig. 8(C), labeled 2, shows the intensity of the shifted plasmon peak (2) in Fig. 8(B) for the Al-rich layer at the alloy/corrosion product interface. Finally, the image, labeled 3, shows the intensity distribution for the broad oxide (MgO) plasmon peak (3 in Fig. 8(B)) located at 22 eV [38].

The position of the EELS peak for the Al-rich layer is close to the plasmon peak for the β-$Mg_{17}Al_{12}$ phase, Fig. 9. The panels in this figure are arranged in a similar order to those in Fig. 8, with the

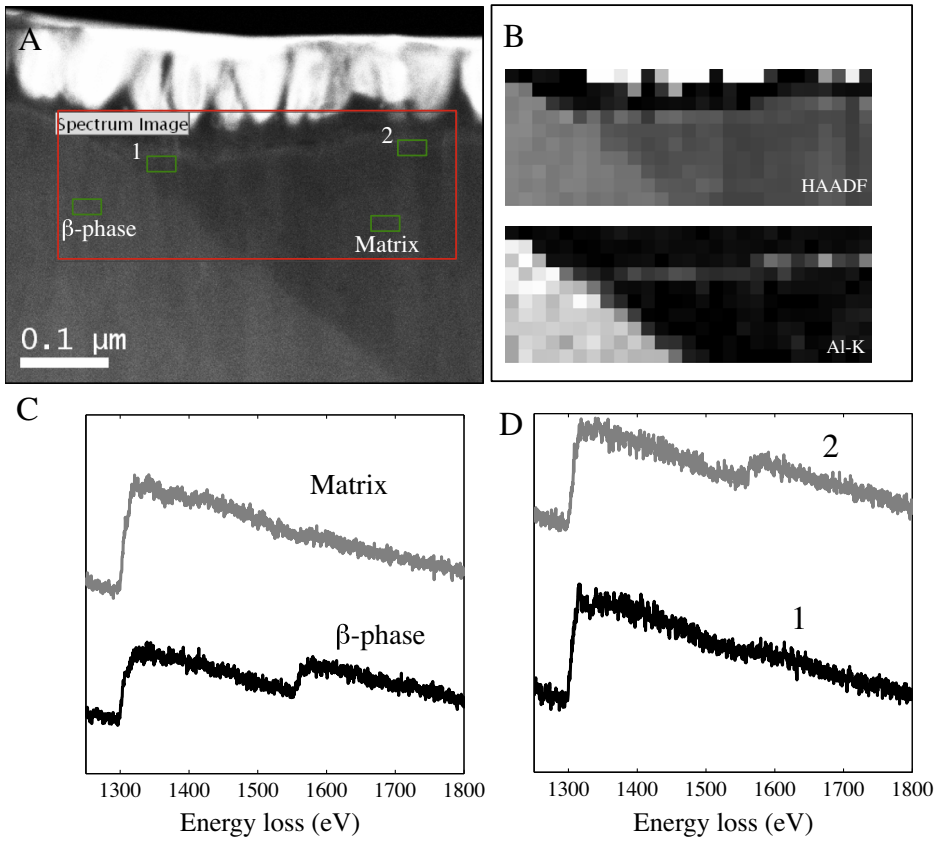

Fig. 10. (A) STEM-HAADF image of the surface layer of area 1. Top image in (B) is the HAADF signal. The lower images in (B) shows the intensity map of the energy range of 1560.8–1818.8 eV (Al). (C and D) Two set of core-loss EELS data, integrated in the same number of horizontal pixels as shown in (A). The plot in (C) presents the spectra from the bulk magnesium matrix and the β-Mg17Al12 phase. The plot in (D) shows two spectra from the surface: spectrum 1 close to the β-phase and spectrum 2 away from it (corresponding areas marked in panel (A)).

HAADF image in (A), spectra in (B), and the intensity maps, and locations at which spectra were recorded, in section (C). Spectra #2 and #3 are acquired from the β-phase and the Al-rich layer, respectively. The full width at half maximum (FWHM) of volume plasmon peaks correlates with the electronic band structure of the material and can provide an indirect insight into the metallic or insulating character of the region [27]. Additional EEL spectra from the Al-rich layer, gathered at higher energy dispersion, are given in Fig. S.2 in the Supplementary section. The plasmon peak for Mg is centered at 10.7 eV with the FWHM of 1.35 eV, while that from the Al-rich layer is located at 12.5 eV with the FWHM of 2.18 eV.

Close inspection of the XEDS map in Fig. 7(D) shows the Al-rich layer disappears close to the intermetallic phase. To determine whether this is meaningful, EELS measurements were performed on either side of the β-phase. The low-loss energy range of the EEL spectrum was presented in Fig. 9. The intensity map shown in the bottom map in Fig. 9(C) corresponds to the shifted plasmon peak (#3) in the Al-rich layer, Fig. 9(B). As observed on the right side of the β-phase, the intensity associated with the Al-rich region is weaker closer to the eutectic β-$Mg_{17}Al_{12}$ phase. (The individual low-loss EEL spectra from this region presented in the supplementary section, Fig. S.3, show this more clearly.) XEDS measurements on the areas surrounding the β-$Mg_{17}Al_{12}$ phase of the partially divorced eutectic microstructure, away from the corroded surface, also demonstrate an aluminum-depleted region adjacent to this eutectic phase (see the supplementary section, Fig. S.4).

As a direct chemical and unequivocal confirmation of the accumulation of Al on the surface, core-loss EELS was performed on the right side of the partially divorced eutectic. The box in Fig. 10(A) shows the area imaged using an HAADF detector. The top image in Fig. 10(B) is the HAADF signal and the lower image is the intensity map for the Al–K edge. The two sets of spectra in Fig. 10(C) and (D) present core-loss EELS data (Mg–K edge at 1305 eV and Al–K edge at 1560 eV) from four different locations. The spectra on panel (C) were recorded on the Mg matrix and within the β-$Mg_{17}Al_{12}$ phase. The plots on panel (D) show spectra for the two locations (1 and 2) indicated in Fig. 10(A). Location 1 was to the immediate right of the β-phase and location 2 was ~300 nm from the β-phase. As can be observed, the signal for the Al–K edge is more intense for the distant location (2) than for the adjacent location (1), confirming the XEDS and low-loss EELS observations.

3.2.2. Area 2 – Primary magnesium grain

Fig. 11(A) and (B) present low and high magnification STEM-HAADF images of the FIB section cut from an α-Mg grain; area 2 in Fig. 4(D). Fig. 11(B) shows the columnar morphology of the oxide/hydroxide layer, which is similar to that present on the section cut from area 1 (Figs. 4 and 5). From the XEDS maps of the area highlighted in panel (B), no indication of an Al-rich layer at the alloy interface can be observed, Fig. 11(C). A signal for Cl, uniformly distributed throughout the oxide is also observed. No Cl signal was observed for area 1. The oxygen signal is uniform across the corrosion layer. Individual XEDS spectra from this region, supporting the presence of these elements, are included in the supplementary section (Fig. S.5). There, it is shown that the top corrosion film contains some Al distributed uniformly across the corrosion layer. Also, the signal for Cl is shown to be present in the spectra.

To probe the crystal structure of the thick corrosion film present at this location, we acquired SAD patterns at 11 locations across

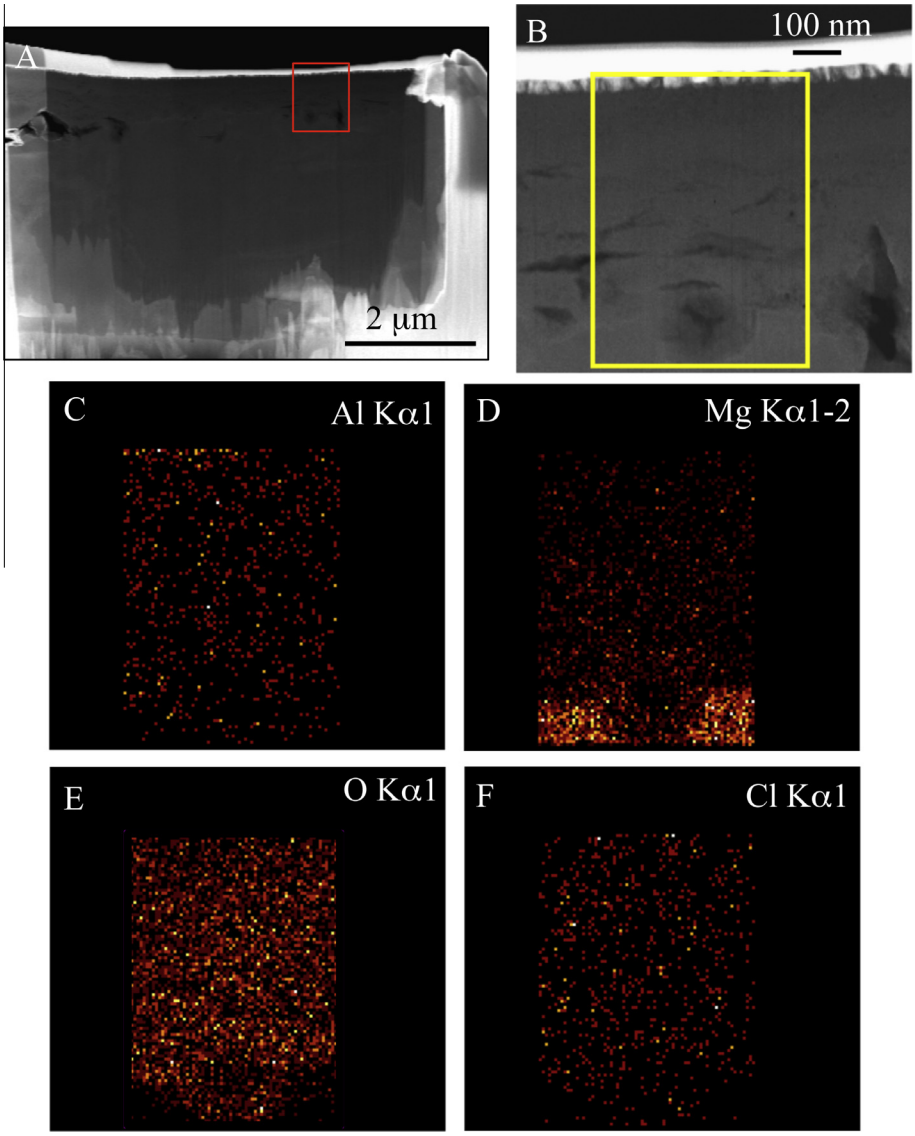

Fig. 11. (A) Low magnification view (STEM-HAADF) of the FIB sample from area 2 in Fig. 4(D), primary α-Mg grain. The area marked with the red box is shown in (B). The region marked in (B) is used for XEDS elemental analysis. XEDS elemental maps are shown in: (C) Al, (D) Mg, (E) O and (F) Cl. (For interpretation of the references to color in this figure legend, the reader is referred to the web version of this article.)

this layer. Fig. 12(A) shows the area analyzed, the initial beam location (1), and the direction over which the patterns shown in Fig. 12(B) were recorded. Fig. 12(B) shows the evolution in the SAD patterns across the corrosion layer. SAD #1 corresponds to the Mg substrate close to the [0001] zone axis (ZA) (see the simulation in #1*). As the electron beam probes areas farther from the Mg substrate, the diffraction ring pattern of MgO appears and the diffraction spots for Mg fade (SAD #2 to #4). In SAD #5 the rings show a discrete and non-uniform intensity distribution, indicating that the crystalline MgO grains are larger in this region. In SAD #6 the diffraction spot is consistent with the 001 reflection of $Mg(OH)_2$ (4.77 Å, marked with an arrow). This diffraction spot quickly disappeared, due to beam exposure. The use of a cryo-holder was very effective in increasing the stability of the $Mg(OH)_2$ phase within the TEM. Even on first exposure of the surface layer to the beam, the $Mg(OH)_2$-001 diffraction spot was the only indication of crystalline hydroxide. Farther away from the Mg substrate, the diffraction rings are consistent with the presence of only MgO (SAD #7 with a simulated MgO ring pattern). Nanocrystalline to fully amorphous regions (SAD #8) are also present. SAD #9 to #11 show the diffraction patterns from the very top section of the corrosion film can also be consistently indexed as MgO.

The phases present within the film were characterized using low-loss EELS measurements. Fig. 13(A) shows the STEM-HAADF image with the numbered locations at which EELS measurements were made. The images in Fig. 13(B) (from left to right) are the HAADF signal, the intensity map corresponding to the Mg volume plasmon peak (10.7 eV), and the intensity map for the oxide plasmon peak (22 eV). Since plural plasmon scattering was observed from the Mg layer due to the thickness of the FIB sample, giving rise to peaks at 21 eV, 32 eV and ~43 eV, we used an energy range for the MgO peak that does not overlap the oxide plasmon peak at 22 eV. Fig. 13(C) and (D) show the site-specific EEL spectra from the locations numbered in Fig. 13(A). The plots on panel (D) show the lower energy loss range. The columnar layer at the very top of the corrosion film (spectrum #1) shows only the peak at 22 eV corresponding to MgO. As the beam approaches the Mg substrate, a secondary peak appears at 8.4 eV (spectra #2 and #3). At locations

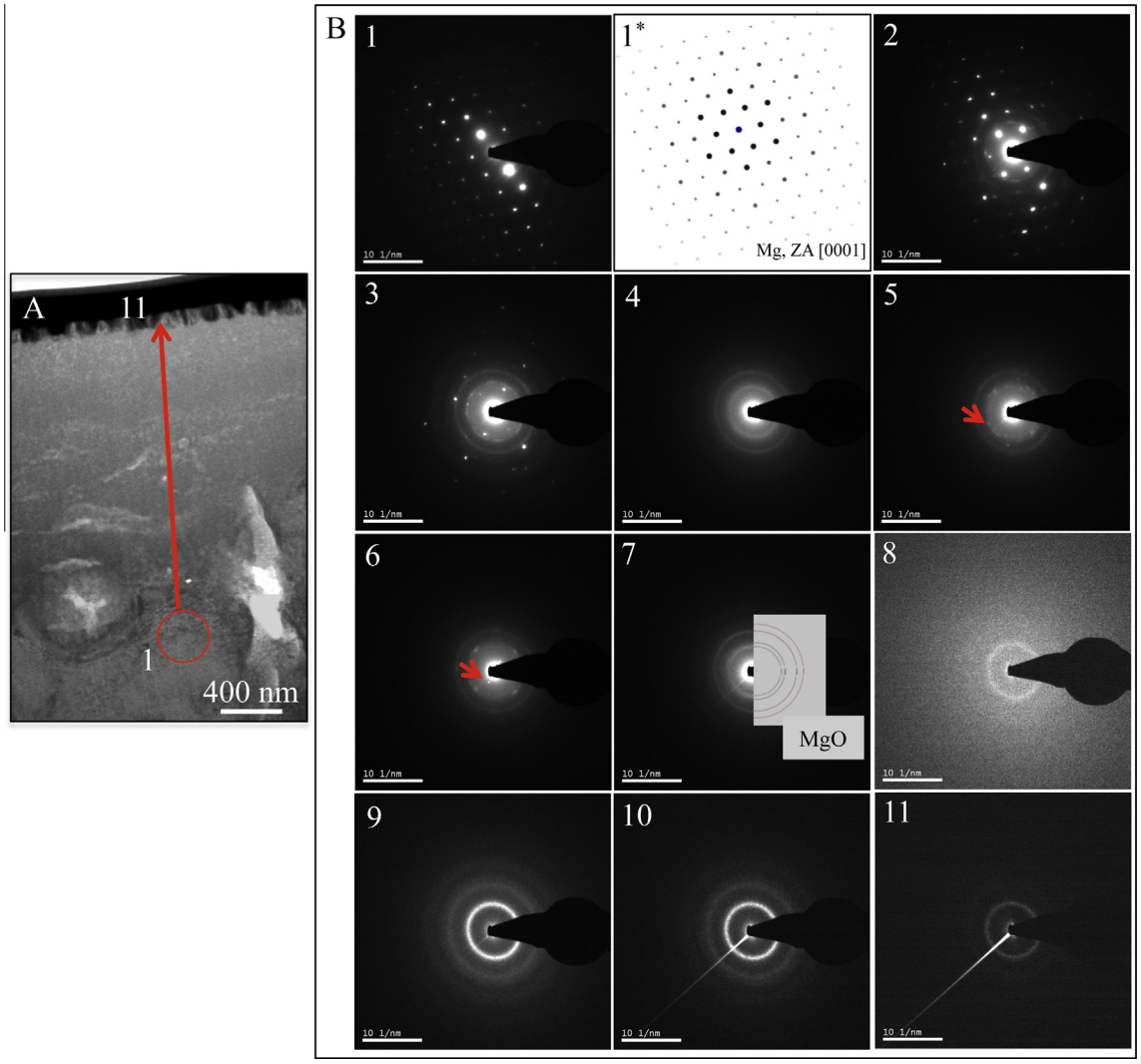

Fig. 12. (A) TEM-BF micrograph of area 2. The area marked 1 shows the selected location for SAD #1. Consecutive SAD's were acquired from #1 to the top columnar layer (#11). (B) SAD patterns and their evolution moving from the base metal to the outer columnar layer. 1^* is the simulation of the spot pattern in 1. The ring pattern is consistently MgO (simulation shown on 7). The arrow in 6 points to a reflection corresponding to 0 0 1-$Mg(OH)_2$.

close to the Mg (spectra #4 and #5), the Mg plasmon peak at 10.7 eV appears. This confirms the observation in XEDS elemental mapping (Fig. 11) that no Al-rich layer is present on the Mg surface beneath the columnar oxide. An additional peak at 13.4 eV is encountered close to the Mg surface (spectra #4 and #5). The spectrum from location #6 shows only the volume plasmon at E_p = 10.7 eV from the Mg matrix. The peak at 8.4 eV has been reported for the low loss spectrum of $Mg(OH)_2$ [39]. This was confirmed by an EELS measurement on a reference $Mg(OH)_2$ powder which yielded a shoulder peak at ~9 eV (data presented in Fig. S.6 in the supplementary section). The slight difference in peak energy can be attributed to the influence of beam exposure on the alloy measurement [33]. Presently, the origin of the peak at 13.4 eV is unknown to us.

4. Discussion

4.1. The Al-rich layer observed in area 1 (close to the eutectic)

The results presented in Figs. 7–10 clearly demonstrate the presence of an Al-rich layer at the alloy/corrosion film interface. The occurrence of such a layer has been reported previously [18–20], and it has been suggested that it is close to amorphous Al_2O_3 [20] and able to enhance corrosion resistance of Mg alloys.

The low-loss EEL spectra from this Al-rich layer (Figs. 8 and 9) are not consistent with these claims, since they exhibit a relatively sharp (FWHM ~ 2 eV) plasmon peak centered close to 12.5 eV, whereas the volume plasmon peak for Al_2O_3 [37], is a broad peak (FWHM = 13 eV) centered at 23.6 eV. The possibility of beam-induced damage is also unlikely, since Al_2O_3 only exhibits electron beam damage at extremely high doses [40]. The possibility that the Al-rich layer was initially aluminum hydroxide, $Al(OH)_3$ [41], can also be ruled out since both pristine and irradiated low-loss peaks for this phase is close to that of Al_2O_3. According to the Drude model [27], the FWHM of the volume plasmon peak is inversely proportional to the relaxation time (τ) of the plasmon resonance. Due to strong damping of the plasma oscillations in non-metallic materials, the relaxation time is generally larger for metallic phases [27]. This results in larger FWHM for ionic/covalent solids, and sharper (smaller FWHM) volume plasmon peaks for metallic phases. This suggests that the Al-rich layer, with a relatively sharp volume plasmon peak (FWHM = 2 eV), is close to metallic in character.

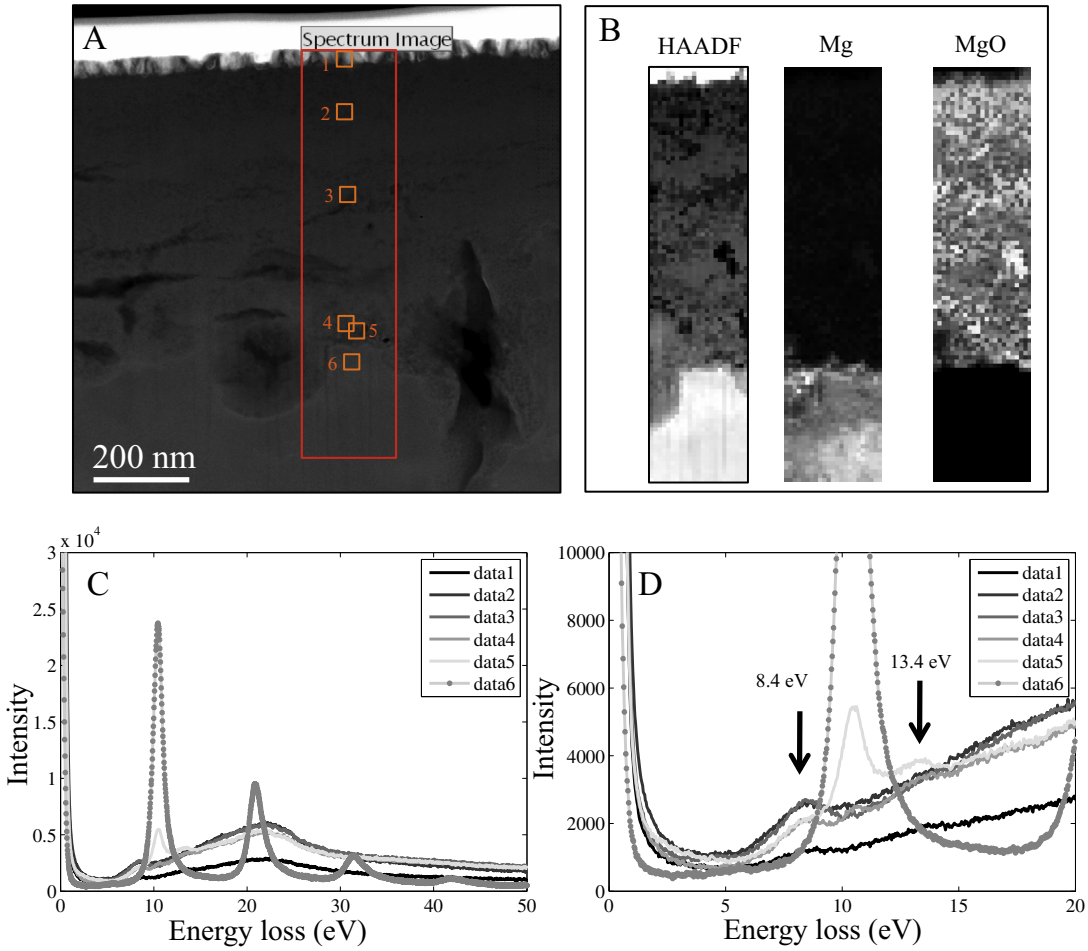

Fig. 13. (A) STEM-HAADF image from area 2 (Fig. 4D). The box shows the area used for spectrum imaging. (B) From left to right: the HAADF signal, intensity map Mg plasmon peak (9.7–11.3 eV), and map for the oxide plasmon peak (14.9–18.5 eV). (C) The low-loss EEL spectra from the marked locations in (A). The plot in panel (D) shows the details of the graph in (C) in the lower energy region of the spectra. (For interpretation of the references to color in this figure legend, the reader is referred to the web version of this article.)

There appear to be two scenarios that could explain the observed location of the plasmon peak for this layer:

(1) This Al-rich layer is formed by the accumulation at the interface of the discontinuously precipitated β-$Mg_{17}Al_{12}$ phase as the corrosion front recedes into the alloy. Characterization of the pristine state of the alloy (Figs. 2 and 3) showed a fine network of precipitated β-phase surrounding the coarse eutectic microstructure. However, comparison of the Al–K edge intensities in the EEL spectra for the β-phase and the Al-rich layer (Fig. 10) indicates the Al content is lower in the latter. A possible explanation would be preferential dissolution of Al from the β-$Mg_{17}Al_{12}$ phase in the corrosion environment. Further investigation is needed to confirm whether this hypothesis can be reconciled with the reported XPS data [20].

(2) A second possibility is that the Al-rich layer is highly defective Al_2O_3. Song et al. [42] speculate that, under corrosion conditions, Al_2O_3 would form as a semiconductor or electronic conductor rather than as a crystalline wide band gap insulator. This could potentially explain the observed sharp plasmon peak, characteristic of the metallic state. The formation of this Al-rich oxide layer can be linked to the higher Al alloy content in this region and the preferential dissolution of Mg during corrosion.

The areas close to the eutectic microstructure, which are devoid of this Al-rich layer (Figs. 9 and 10), are difficult to explain by the first mechanism, without invoking unlikely arguments that the absence of this layer is an artifact of the analysis. A strong argument in favor of the second explanation is that XEDS analyses in the pristine (uncorroded) section of the microstructure, surrounding the partially divorced eutectic (Fig. S.4 in the supplementary section), show that the Mg matrix adjacent to the β-$Mg_{17}Al_{12}$ is devoid of Al in the corroded section of the surface. Based on these arguments the most likely mechanism of formation of the Al-rich layer is by preferential Mg dissolution leading to the accumulation of Al at the alloy/corrosion film interface. The absence of this layer at locations close to the divorced eutectic reflects the lower levels of Al present in the eutectic Mg matrix at these locations.

The uniformity of the corrosion product layer on the eutectic Mg matrix and the β-$Mg_{17}Al_{12}$ eutectic phase suggests that the β-phase may not act as a highly active cathode. This observation is in agreement with the claim that the intermetallic β-phase is only slightly more noble than the α-Mg, with essentially the same corrosion rate [7]. Surface potential maps, acquired using scanning Kelvin probe force microscopy measurements, also suggest that the galvanic couple formed between the α-Mg grain and the β-phase is not of significant strength [43]. The ability of the β-phase to act as a cathode would be expected to be related to the Al con-

tent of the Mg matrix phase: the higher the Al content in solid solution in the Mg grain, the smaller the electrochemical difference between the two phases [7] and the less likely galvanic coupling between a Mg anode and a β-phase cathode.

4.2. The structure of the corrosion film in area 2 (primary α-Mg)

At this location the corrosion film was significantly thicker (~1.5 to 2 μm) compared to that of location 1 (150–200 nm). A layer with a columnar morphology and a similar thickness to that at location 1 is present on the outside of the thicker sublayer of MgO and $Mg(OH)_2$. Electron diffraction measurements, Fig. 12, show the $Mg(OH)_2$ is present closer to the Mg substrate.

This thick corrosion product was evenly permeated with chloride, strongly suggesting that it did not prevent continuous access of the chloride solution to the α-Mg substrate through the full corrosion exposure period. This contrast to the thin oxide at location 1, which contained no detectable chloride, confirms the protective nature of the oxide at locations where the thin Al-rich layer is present. The absence of the Al-rich layer can be attributed to the low Al content of the α-Mg at this location, which was measured to be around 2–3 wt.%. This is significantly lower than that of the eutectic Mg matrix at location 1 which, away from the eutectic β-$Mg_{17}Al_{12}$, was close to 11–12 wt.% Al (Fig. S.4 in the supplementary section).

It is conceivable that the mechanism through which the columnar sections of the corrosion film in areas 1 and 2 are formed are similar, resulting from deposition or precipitation of corrosion products onto the surface. The same process was postulated by Nordlien et al. [16] for the case of formation of the platelets in the top section of the corrosion layer of Mg in water.

5. Conclusions

The detailed electron microscopic analysis of the corroded surface of the sand cast AM50 alloy has been performed. Two representative areas were analyzed: (i) a location close to a divorced eutectic microstructure where the extent of corrosion was minor; and (ii) an area located on an α-Mg grain where corrosion was extensive.

At the lightly corroded area, the outer regions of the corrosion film were comprised of a columnar mixture of amorphous MgO and $Mg(OH)_2$. Beneath this layer, at the alloy/oxide interface, a thin Al-rich layer was observed. This layer was metallic in character and is most likely a highly defective Al_2O_3 formed by the preferential dissolution of Mg from the alloy at this location which has a high Al content (11–12 wt.%).

On the heavily corroded area, located on an α-Mg grain, the thick corrosion product layer is predominantly crystalline MgO and $Mg(OH)_2$. The absence of the Al-rich layer at this location allows corrosion to progress uninhibited. The inability of the surface to form the Al-rich layer can be attributed to the low Al content of the α-Mg grain (2–3 wt.%) at this location.

Acknowledgements

Funding for this research was provided by General Motors Canada and the Natural Sciences and Engineering Research Council of Canada (NSERC). The authors thank Ms. Julia Huang, Mr. Chris Butcher, and Mr. Andy Duft for their invaluable technical support during the course of this work. The microscopy work was carried out at the Canadian Centre for Electron Microscopy, a facility supported by NSERC and McMaster University.

Appendix A. Supplementary material

Supplementary data associated with this article can be found, in the online version, at http://dx.doi.org/10.1016/j.corsci.2013.07.038.

References

[1] I.J. Polmear, Recent developments in light alloys, Materials Transactions, JIM 37 (1) (1996) 12–31.
[2] M.O. Pekguleryuz, A.A. Kaya, Creep resistant magnesium alloys for powertrain applications, Advanced Engineering Materials 5 (12) (2003) 866–878.
[3] R.E. McNulty, J.D. Hanawalt, Some corrosion characteristics of high purity magnesium alloys, Transactions of The Electrochemical Society 81 (1) (1942) 423–433.
[4] H. Matsubara, Y. Ichige, K. Fujita, H. Nishiyama, K. Hodouchi, Effect of impurity Fe on corrosion behavior of AM50 and AM60 magnesium alloys, Corrosion Science 66 (2013) 203–210.
[5] A.D. Südholz, N.T. Kirkland, R.G. Buchheit, N. Birbilis, Electrochemical properties of intermetallic phases and common impurity elements in magnesium alloys, Electrochemical and Solid-State Letters 14 (2) (2012) C5–C7.
[6] R. Lindström, J.-E. Svensson, L.-G. Johansson, The influence of carbon dioxide on the atmospheric corrosion of some magnesium alloys in the presence of NaCl, Journal of Electrochemical Society 149 (4) (2002) B103–B107.
[7] S. Mathieu, C. Rapin, J. Steinmetz, P. Steinmetz, A corrosion study of the main constituent phases of AZ91 magnesium alloys, Corrosion Science 45 (2003) 2741–2755.
[8] S. Feliu Jr., A. Pardo, M.C. Merino, A.E. Coy, F. Viejo, R. Arrabal, Correlation between the surface chemistry and the atmospheric corrosion of AZ31, AZ80 and AZ91D magnesium alloys, Applied Surface Science 255 (2009) 4102–4108.
[9] G.L. Makar, J. Kruger, Corrosion studies of rapidly solidified magnesium alloys, Journal of the Electrochemical Society 137 (2) (1990) 414–421.
[10] G. Song, A.L. Bowles, D.H. StJohn, Corrosion resistance of aged die cast magnesium alloy AZ91D, Materials Science and Engineering A 366 (1) (2004) 74–86.
[11] G.L. Song, A. Atrens, Corrosion mechanisms of magnesium alloys, Advanced Engineering Materials 1 (1) (1999) 11–33.
[12] G. Song, A. Atrens, M. Dargusch, Influence of microstructure on the corrosion of diecast AZ91D, Corrosion Science 41 (1998) 249–273.
[13] M.-C. Zhao, M. Liu, G. Song, A. Atrens, Influence of the β-phase morphology on the corrosion of the Mg alloy AZ91, Corrosion Science 50 (2008) 1939–1953.
[14] A. Pardo, M.C. Merino, A.E. Coy, R. Arrabal, F. Viejo, E. Matykina, Corrosion behaviour of magnesium/aluminium alloys in 3.5 wt.% NaCl, Corrosion Science 50 (2008) 823–834.
[15] M.C. Merino, A. Pardo, R. Arrabal, S. Merino, P. Casajus, M. Mohedano, Influence of chloride ion concentration and temperature on the corrosion of Mg–Al alloys in salt fog, Corrosion Science 52 (2010) 1696–1704.
[16] J.H. Nordlien, S. Ono, N. Masuko, K. Nicancioglu, Morphology and structure of oxide films formed on magnesium by exposure to air and water, Journal of the Electrochemical Society 142 (10) (1995) 3320–3322.
[17] J.H. Nordlien, S. Ono, N. Masuko, K. Nisancioglu, A TEM investigation of naturally formed oxide films on pure magnesium, Corrosion Science 39 (1997) 1397–1414.
[18] J.H. Nordlien, K. Nisancioglu, S. Ono, N. Masuko, Morphology and structure of oxide films formed on MgAl alloys by exposure to air and water, Journal of the Electrochemical Society 143 (8) (1996) 2564–2572.
[19] S.J. Splinter, N.S. McIntyre, The initial interaction of water vapour with Mg–Al alloy surfaces at room temperature, Surface Science 314 (1994) 157–171.
[20] L. Wang, T. Shinohara, B.-P. Zhang, XPS study of the surface chemistry on AZ31 and AZ91 magnesium alloys in dilute NaCl solution, Applied Surface Science 256 (2010) 5807–5812.
[21] S. Feliu Jr, M.C. Merino, R. Arrabal, A.E. Coy, E. Matykina, XPS study of the effect of aluminium on the atmospheric corrosion of the AZ31 magnesium alloy, Surface and Interface Analysis 41 (2009) 143–150.
[22] L.P.H. Jeurgens, M.S. Vinodh, E.J. Mittemmeijer, Initial oxide-film growth on Mg-based MgAl alloys at room temperature, Acta Materialia 56 (2008) 4621–4634.
[23] D. Sachdeva, Insights into microstructure based corrosion mechanism of high pressure die cast AM50 alloy, Corrosion Science 60 (2012) 18–31.
[24] ASTM Standard B275, Standard Practice for Codification of Certain Nonferrous Metals and Alloys, Cast and Wrought. ASTM International, West Conshohocken, PA, 2005, doi: http://dx.doi.org/10.1520/B0275-05, <http://www.astm.org>.
[25] S. Xu, V.Y. Gertsman, J. Li, J.P. Thomson, M. Sahoo, Role of mechanical twinning in tensile compressive yield asymmetry of die cast Mg alloys, Canadian Metallurgical Quarterly 44 (2) (2005) 155–166.
[26] K.B. Deshpande, Validated numerical modeling of galvanic corrosion for couples: magnesium alloy (AE44)-mild steel and AE44-aluminum alloy (AA6063) in brine solution, Corrosion Science 52 (2010) 3514–3522.
[27] R.M. Asmussen, P. Jakupi, M. Danaie, G.A. Botton, D.W. Shoesmith, Tracking the corrosion of magnesium sand cast AM50 alloy in chloride environments, Corrosion Science 75 (2013) 114–122.

[28] R.F. Egerton, Electron Energy-Loss Spectroscopy in the Electron Microscope, third ed., Springer, New York, 2011.
[29] A.K. Dahle, Y.C. Lee, M.D. Nave, P.L. Schaffer, D.H. StJohn, Development of the as-cast microstructure in magnesium–aluminium alloys, Journal of Light Metals 1 (2001) 61–72.
[30] X.J. Liu, I. Ohnuma, R. Kainuma, K. Ishida, Thermodynamic assessment of the aluminum-manganese (Al–Mn) binary phase diagram, Journal of Phase Equilibria 20 (1) (1999) 45–56.
[31] B.L. Mordike, P. Lukac, Physical Metallurgy, in: H.E. Friedrich, B.L. Mordike (Eds.), Magnesium Technology; Metallurgy, Design Data, Applications, Springer, 2006, p. 85.
[32] H. Westengen, T.K. Aune, Magnesium Casting Alloys, in: H.E. Friedrich, B.L. Mordike (Eds.), Magnesium Technology; Metallurgy, Design Data, Applications, Springer, 2006, p. 156.
[33] S. Barbagallo, H.I. Laukli, O. Lohne, E. Cerri, Divorced eutectic in a HPDC magnesium–aluminum alloy, Journal of Alloys and Compounds 378 (2004) 226–232.
[34] M.-X. Zhang, P.M. Kelly, Crystallography of $Mg_{17}Al_{12}$ precipitates in AZ91D alloy, Scripta Materialia 48 (2003) 647–652.
[35] M. Taheri, R.C. Phillips, J.R. Kish, G.A. Botton, Analysis of the surface film formed on Mg by exposure to water using a FIB cross-section and STEM–EDS, Corrosion Science 59 (2012) 222–228.
[36] N.J. Zaluzec, T. Schober, D.G. Westlake, in: Proceedings of the Annual Meeting of the Electron Microscopy Society of America (39th Annual EMSA Meeting), Electron Microscopy Society of America: Atlanta, GA, 1981, pp 194–195.
[37] M. Danaie, S.X. Tao, P. Kalisvaart, D. Mitlin, Analysis of deformation twins and the partially dehydrogenated microstructure in nanocrystalline magnesium hydride (MgH_2) powder, Acta Materialia 58 (2010) 3162–3172.
[38] Data for low-loss EELS of MgO and Al_2O_3 from the EELS Atlas provided, in: C.C. Ahn (Ed.), Transmission Electron Energy Loss Spectroscopy in Materials Science and the EELS Atlas, Weinheim, Wiley-VCH, 2005.
[39] D. Su, N. Jiang, J.C.H. Spence, F. He, W.T. Petuskey, On the dehydration mechanism of $Mg(OH)_2$ by a high-energy electron beam, Journal of Applied Physics 104 (2008) 063514.
[40] G.P. Pells, D.C. Phillips, Radiation damage of α-Al_2O_3 in the HVEM: II, Radiation damage at high temperature and high dose, Journal of Nuclear Materials 80 (1979) 215–222.
[41] N. Jiang, J.C.H. Spence, In situ EELS study of dehydration of $Al(OH)_3$ by electron beam irradiation, Ultramicroscopy 111 (2011) 860–864.
[42] G. Song, A. Atrens, X. Wu, B. Zhang, Corrosion behaviour of AZ21, AZ501 and AZ91 in sodium chloride, Corrosion Science 40 (10) (1998) 1769–1791.
[43] A. Pardo, M.C. Merino, A.E. Coy, F. Viejo, R. Arrabal, S. Feliu Jr., Influence of microstructure and composition on the corrosion behaviour of Mg/Al alloys in chlorine media, Electrochimica Acta 53 (2008) 7890–7902.